# Anisotropic Magnetic Field–Temperature Phase Diagrams in CeCoSi

Hiroyuki Hidaka[1 *], Shun Yanagiya[1], Shintaro Onodera[1], Tatsuya Yanagisawa[1], Hiroshi Amitsuka[1], Hiroshi Tanida[2], and Takayuki Ishitobi[3]

[1]*Graduate School of Science, Hokkaido University, Sapporo, Hokkaido 060-0810, Japan*
[2]*Liberal Arts and Sciences, Toyama Prefectural University, Imizu, Toyama 939-0398, Japan*
[3]*ASRC, Japan Atomic Energy Agency, Tokai, Ibaraki 319-1195, Japan*

The Ce-based metallic compound CeCoSi with a tetragonal structure exhibits an antiferromagnetic ordering at $T_N$ = 9.4 K and a nonmagnetic (NM) ordering accompanied by a uniform lattice distortion at $T_0 \sim 12$ K. A magnetic field ($H$)-induced phase transition accompanied by a change in the crystal structure occurs at an ordering temperature of $T_{s1}$ in the NM ordering state for $H \parallel [100]$ [Matsumura et al., J. Phys. Soc. Jpn. **91**, 064704 (2022)]. To construct detailed magnetic field–temperature ($H$–$T$) phase diagrams of this compound, including the $H$ dependence of $T_{s1}$ near the zero field, we have performed magnetization, electrical resistivity, and specific heat measurements under $H$ parallel to the [100] and [110] directions. The present bulk measurements indicate that the $T_{s1}$ transition is absent for $H \parallel [110]$. Furthermore, it can be deduced that $T_{s1}$, observed only for $H \parallel [100]$, coincides with $T_0$ at zero field. The revealed anisotropic phase diagrams offer valuable insights into the symmetry of the order parameter in the nontrivial NM ordering of CeCoSi.

## 1. Introduction

The identification of the order parameter (OP) is essential for the description of an ordered state in materials. However, there are several materials, such as $URu_2Si_2$, that exhibit an ordering whose OP is unidentified, called hidden ordering (HO).[1,2] In general, various investigations including microscopy measurements such as nuclear magnetic resonance (NMR) and resonant X-ray scattering are required to unveil the OP of HO. Among these approaches, the construction of a detailed phase diagram is one of the crucial approaches, as it can provide insights into the symmetry of the relevant OPs. In fact, anisotropic magnetic phase diagrams depending on the symmetry of OP have been constructed for various materials, such as electric quadrupole ordering systems.[3–9]

The Ce-based intermetallic compound CeCoSi has been intensively studied in recent years as a material exhibiting an enigmatic ordering. It crystallizes in the nonsymmorphic tetragonal structure with $P4/nmm$.[10] In this structure, the space-inversion symmetry is locally broken at each atomic site, although the crystal structure is centrosymmetric. CeCoSi undergoes two successive phase transitions at low temperatures: an antiferromagnetic (AFM) ordering derived from $4f$ electrons at $T_N$ = 9.4 K and a nonmagnetic (NM) ordering at $T_0 \sim 12$ K.[11–15] From neutron diffraction measurements, the propagation vector of this AFM ordering has been determined to be $\boldsymbol{q} = 0$.[16] On the other hand, the $^{59}$Co nuclear quadrupole resonance (NQR) measurements of a single crystal of CeCoSi revealed the NM feature between $T_0$ and $T_N$.[17] In this paper, this NM ordering whose OP has not yet been identified is denoted as HO. It has been known that $T_0$ increases with the magnetic field $H$ in a magnetic field–temperature ($H$–$T$) phase diagram.[11,12,15] These features are reminiscent of an antiferroquadrupole (AFQ) ordering of the $4f$ electrons.[3,18,19] However, for CeCoSi, a crystalline-electric-field (CEF) level scheme for the $4f^1$ configuration in $Ce^{3+}$ with the $4mm$ ($C_{4v}$) symmetry has been proposed to be the $\Gamma_7^{(1)}$ doublet ground state and the $\Gamma_7^{(2)}$ and $\Gamma_6$ excited doublets located at 125 and 165 K, respectively.[16,20] In this CEF level scheme, the electric quadrupole degrees of freedom exist only between two CEF levels, which are largely separated, as the interorbital degrees of freedom.[21] This is different from the $\Gamma_8$ quartet ground state in $CeB_6$ and the non-Kramers $\Gamma_3$ doublet ground state in $PrPb_3$ with the quadrupole degrees of freedom in cubic cases.[3,18,19]

The contribution of Co-$3d$ electrons to the physical properties of CeCoSi has also been pointed out. The conduction bands in CeCoSi are considered to consist mainly of Co-$3d$ electrons.[22] The effective moment in CeCoSi has been estimated to be $\sim 3.3\ \mu_B$/Ce, which is larger than that expected for the free $Ce^{3+}$ ion. This can be attributed to the contribution of the Pauli paramagnetic susceptibility coming from the Co-$3d$ electrons, since the large effective moment approaches the expected value for the free $Ce^{3+}$ by subtracting the paramagnetic susceptibility of LaCoSi.[12] In addition, an estimated Sommerfeld coefficient $\gamma$ for CeCoSi appears to be nearly the same as that (18 mJ mol$^{-1}$ K$^{-2}$) for LaCoSi.[11,12] Note that CeCoSi shows no magnetic ordering derived from the Co-$3d$ electrons,[12,17] in contrast to the isostructural metallic compound CeMnSi showing an AFM ordering of Mn-$3d$ electrons.[23]

Recent vigorous research has made significant strides in understanding the HO in CeCoSi,[12,15–17,20,24–27] but its origin remains to be elucidated. One of the open issues is the origin of a uniform lattice distortion associated with the HO, which has been suggested to be a triclinic distortion based on recent X-ray diffraction (XRD) measurements of a single crystal of CeCoSi.[24] Another open issue is the interpretation of the anisotropic $H$–$T$ phase diagram. We have reported the $H$–$T$ phase diagrams for $H \parallel [100]$ and [001] from bulk measurements under high $H$ up to 14 T.[15] Here, the paramagnetic (PM), HO, and AFM phases are referred as I, II, and III, respectively. In addition, Matsumura et al. have reported the $H$–$T$ phase diagrams for $H \parallel [100]$ and [110] based on the XRD measurements up to 6 T.[24] It is significant that the $H$–$T$ phase diagram for $H \parallel [100]$ presented in both reports shows

*hidaka@phys.sci.hokudai.ac.jp

an $H$-induced phase in the HO state, named II'. The transition point between phases II and II' is termed $T_{s1}$.[28] It has been suggested that the crystal system of phase II' is higher than triclinic.[24]

The anisotropy of the $H$–$T$ phase diagrams observed in CeCoSi should be an important key to solving the HO puzzle. It remains unclear how the $T_{s1}$ phase boundary behaves near zero magnetic field, such as, whether it coincides with $T_0$ at zero field, which will provide essential information about the symmetry of each phase. In this study, we have performed precise measurements of the electrical resistivity $\rho$, magnetization $M$, and specific heat $C$ under $H \parallel [100]$ and [110] for single crystals of CeCoSi in high magnetic fields up to 14 T. Moreover, we have compiled the $H$–$T$ phase diagrams constructed from the bulk measurements with respect to the major crystal axes by adding the results under $H \parallel [100]$ and [001] reported previously.[15]

In this paper, the experimental results are presented in Sect. 3: the results of $M$ and $\rho$ under $H \parallel [110]$ up to 14 T in Sect. 3.1, and the results of $M$ and $C$ in the low $H$ region for $H \parallel [100]$ and [110] in Sect. 3.2. In addition, we summarize the $H$–$T$ phase diagrams and discuss the ordered states of CeCoSi in Sect. 4. We provide an overview of the $H$–$T$ phase diagram in Sect. 4.1, phases II and II' at low fields in Sect. 4.2, an interpretation of the anisotropic $H$–$T$ phase diagrams based on Landau's theory in Sect. 4.3, and open issues in Sect. 4.4.

## 2. Experimental Details

Single crystals of CeCoSi have been prepared by a Ce/Co eutectic flux method as described in a previous paper.[12] This study has been carried out on two sample pieces, named #1 and #2, taken from different batches. The masses of the thin plate-like samples of #1 and #2 with a thickness of ~ 0.4 mm are ~ 2.7 and 12.5 mg, respectively. Note that the present sample piece named #1 is the same one used in our previous $\rho$, $C$, and $M$ measurements under $H \parallel [100]$ and [001], where $T_0$ and $T_N$ were determined to be ~ 13.2 and 9.3 K at zero magnetic field, respectively.[15] The small residual resistivity of ~3 $\mu\Omega$cm in sample #1 guarantees the high quality of the present sample.[15]

The $\rho$ of sample #1 was measured by a conventional four-probe method in the temperature range of 2–300 K and in the magnetic field range up to 14 T using a physical property measurement system (PPMS; Quantum Design). Electric current and a magnetic field were applied along the [100] and [110] directions, respectively. DC $M$ measurements were performed in the temperature range of 2–300 K and in the magnetic-field range of 0.05–7 T using a magnetic property measurement system (MPMS3; Quantum Design) with $H$ applied along the [110] direction for sample #1 and along the [100] and [110] directions for sample #2. For sample #2, $C$ measurements were also performed by a thermal-relaxation method near $T_0$ at magnetic fields below 5 T using the PPMS, with $H$ applied parallel to [100] and [110].

## 3. Experimental Results

### *3.1 H ∥ [110] in the high-H region*

#### *3.1.1 Magnetization*

Figure 1 shows the temperature dependence of the magnetic susceptibility [= $M(T)/H$] below 20 K in CeCoSi (sample #1) for $H \parallel [110]$ in magnetic fields up to 7 T. An upward

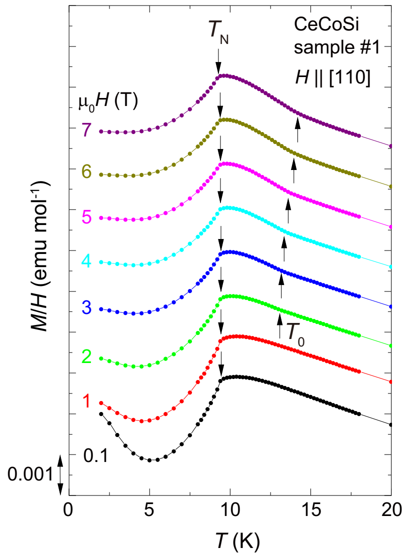


**Fig. 1.** (Color online) Temperature dependence of magnetic susceptibility [= $M(T)/H$] in CeCoSi (sample #1) under $H \parallel [110]$ below 20 K in magnetic fields up to 7 T. The data are shifted vertically for ease of viewing. For their absolute values, refer to the data shown in Fig. 2.

bend at $T_0$ is observed in these $M(T)/H$ curves above 2 T, whereas a clear kink is observed at $T_N$ in all curves. $T_0$ increases with $H$, whereas $T_N$ decreases. Here, $T_0$ and $T_N$ were determined from maximum and minimum, respectively, of the second derivative of $M(T)/H$ [see Fig. S5 in the Supplemental Materials (SM)].[29]

Figures 2(a) and 2(b) show $M(T)/H$ vs $T$ on sample #1 below 30 K for $H \parallel [100]$, [110], and [001] at $\mu_0 H = 1$ and 7 T. Here, the data for $H \parallel [100]$ and [001] are taken from a previous paper.[15] The $M(T)/H$ curves in all $H$ directions show the Curie–Weiss behavior at high temperatures, and $M(T)/H$ for [001] is larger than those for [100] and [110], as seen in the inset of Fig. 2(a). Note that the slight difference in $M(T)/H$ between [100] and [110] in the PM state may be due to experimental error. The $M(T)/H$ curves near $T_0$ are similar between [100] and [110]. On the other hand, the kink at $T_N$ observed at 1 T changes to a dip anomaly only under $H \parallel [100]$ at 7 T. In addition, the steep decrease in $M(T)/H$ below $T_N$ is suppressed only under $H \parallel [100]$, suggesting that the magnetic moments are perpendicular to the [100] direction in the AFM phase at high fields.

Figures 3(a) and 3(b) show the magnetization processes $M(H)$ of CeCoSi (sample #1) and their derivatives $dM/dH$, respectively, for $H \parallel [110]$ up to 7 T, measured at temperatures between 2 and 20 K. The data in Fig. 3(a) are vertically shifted for clarity. The $M(H)$ curves for $H \parallel [110]$ show a simple linear behavior in the PM state; however, a slight deviation from the linear behavior can be seen below $T_0$, as observed in the measurements under other $H$ directions.[15] This deviation is more pronounced in the derivative data. Here, the steep decrease in $dM/dH$ near zero field was also observed in the previous results for $H \parallel [100]$ and [001], which may be due to magnetic impurity.

The $dM(H)/dH$ data at 16 K are almost independent of $H$, whereas at 14 K, it begins to increase above about 6 T, indicating that the system is approaching the HO state. Below $T_0$, determined at zero field (~ 13.3 K), the $dM(H)/dH$ curves

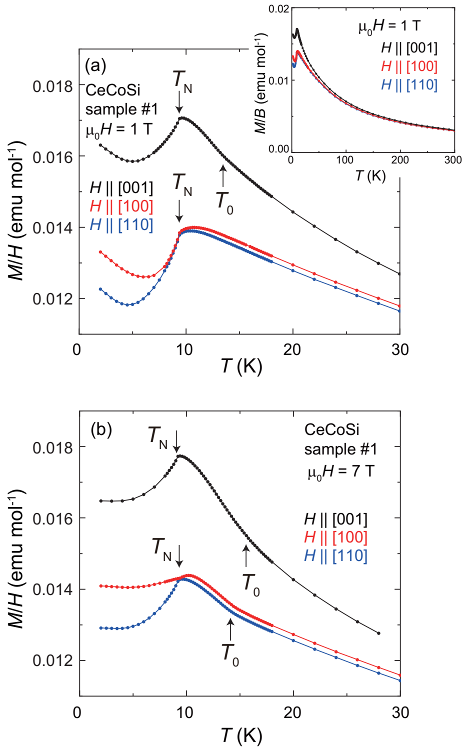


**Fig. 2.** (Color online) $M(T)/H$ vs $T$ in CeCoSi (sample #1) below 30 K under $H \parallel$ [100], [110], and [001] at $\mu_0 H$ = (a) 1 T and (b) 7 T. The inset of (a) shows the data below 300 K at $\mu_0 H$ = 1 T. Here, the $M(T)/H$ data under $H \parallel$ [100] and [001] are taken from a previous paper.[15)]

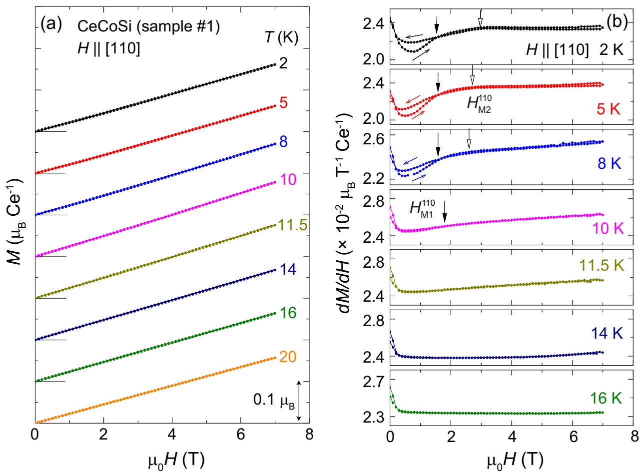


**Fig. 3.** (Color online) (a) Magnetization curves of CeCoSi (sample #1) for $H \parallel$ [110] at several temperatures below 20 K. The data are shifted by 0.1 $\mu_B$/Ce with respect to each other for ease of viewing. (b) Their respective derivatives $dM/dH$. The colored arrows near the hysteresis in (b) represent the increasing and decreasing $H$ processes.

show a bend at $H_{M1}^{110}$. Here, $H_{M1}^{110}$ is defined as the magnetic field where the bend occurs in the $H$ increasing process. In the AFM state, the $dM/dH$ curves show another bend at $H_{M2}^{110}$ ~ 3 T in addition to the anomaly accompanied by hysteresis below $H_{M1}^{110}$. The obtained $T_0$, $T_N$, $H_{M1}^{110}$, and $H_{M2}^{110}$ are summarized in the $H$–$T$ phase diagram (see Fig. 5). $H_{M1}^{110}$ increases slightly with increasing temperature, whereas $H_{M2}^{110}$ decreases. $H_{M1}^{110}$ appears to persist in the HO phase, although these bending anomalies become less distinct with increasing temperature.

### *3.1.2 Electrical resistivity*

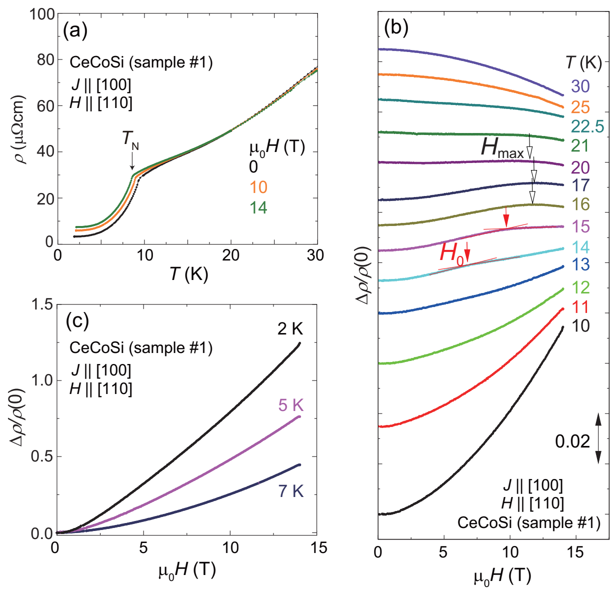


**Fig. 4.** (Color online) (a) Temperature dependence of the electrical resistivity $\rho(T)$ in CeCoSi (sample #1) at 0, 10, and 14 T. $\Delta\rho/\rho(0)$ plotted as a function of $H$ at several temperatures in the range (b) between 10 and 30 K and (c) below 7 K. In (b), the data are shifted vertically for ease of viewing. The electric current $J$ was applied along the [100] axis, whereas $H$ was applied along the [110] axis.

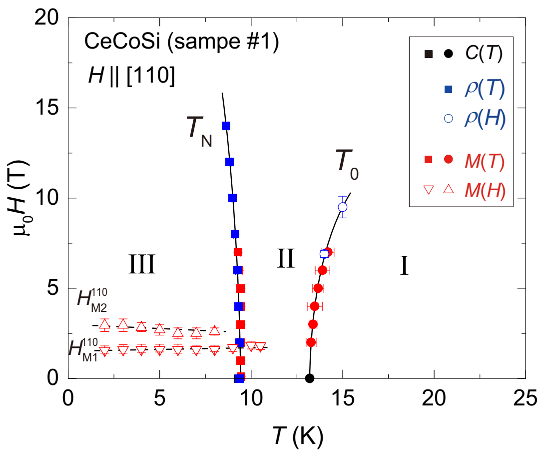


**Fig. 5.** (Color online) Magnetic field–temperature phase diagram of CeCoSi constructed on the basis of the present $\rho$ and $M$ measurements using sample #1 under $H \parallel$ [110]. The data obtained from the previous $C$ measurements at zero magnetic field are also plotted.[15)] The solid and dashed curves are guides for the eye.

Figure 4(a) shows the temperature dependence of the electrical resistivity $\rho(T)$ below 30 K at magnetic fields up to 14 T in CeCoSi (sample #1). Here the electric current $J$ was applied along the [100] direction and $H$ along the [110] direction. The residual resistivity ratio $RRR = \rho_{300K}/\rho_0$ is evaluated to be ∼ 63. The $\rho(T)$ data at zero field show a slight decrease below $T_0$ and a clear kink anomaly at $T_N$, which is in good agreement with that reported previously.[12,15] The anomaly at $T_0$ is unclear even at high magnetic fields, similar to the results for $H$ parallel to [100] and [001], whereas the decrease below $T_N$ is clearly observed.

The results of magnetoresistance (MR) measurements of CeCoSi (sample #1) under $J \parallel [100]$ and $H \parallel [110]$ in the $H$ region up to 14 T above and below $T_N$ are shown in Figs. 4(b) and 4(c), respectively. Here, $\Delta\rho(H)$ and $\rho(0)$ are defined as $[\rho(H) - \rho(0)]$ and $\rho$ at $H = 0$ at a fixed temperature, respectively. In Fig. 4(b), the data are shifted vertically for clarity.

In Fig. 4(b), below 13 K, corresponding to the HO state, $\Delta\rho(H)/\rho(0)$ shows a monotonic increase with $H$. At 14 and 15 K, one can see a kink anomaly at $\mu_0 H \sim 6.9$ and 9.5 T, respectively. The corresponding magnetic field where the kink anomaly appears, defined as $H_0$, is considered to be the transition from the PM state to the HO since the $H_0(T)$ curve merges with the $T_0(H)$ curve in the $H$–$T$ phase diagram [blue open circle in Fig. 5]. The kink anomaly at $H_0$ gradually changes to a maximum at $H_{max}$ above 16 K. The maximum cannot simply be regarded as a transition from the PM state to the HO since $H_{max}$ is almost independent of temperature. Above 25 K, $\Delta\rho(H)/\rho(0)$ shows a monotonic decrease with increasing $H$, which should be due to the suppression of magnetic scattering between the 4$f$ electrons and the conduction electrons by the external $H$. A similar sign change from a positive to negative MR was also found in previous MR measurements under $H \parallel [100]$.[15]

The results of $\Delta\rho(H)/\rho(0)$ for $H \parallel [110]$ in the AFM state are shown in Fig. 4(c). These $\Delta\rho(H)/\rho(0)$ curves show a positive MR. There is no clear anomaly in the MR curves near $H_{M1}^{110}$ and $H_{M2}^{110}$ determined from the present $M(H)$ measurements.

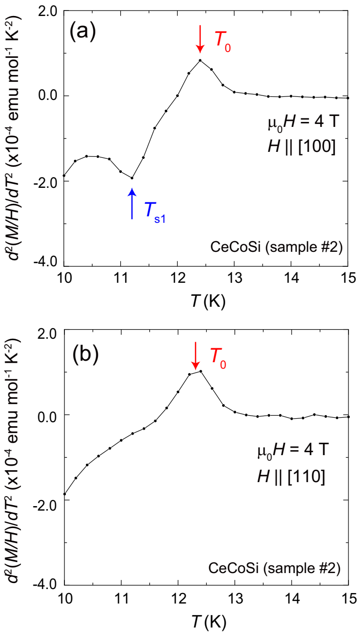


**Fig. 6.** (Color online) Second derivative of $M(T)/H$ with respect to temperature in CeCoSi (sample #2) for $H \parallel$ (a) [100] and (b) [110] at 4 T.

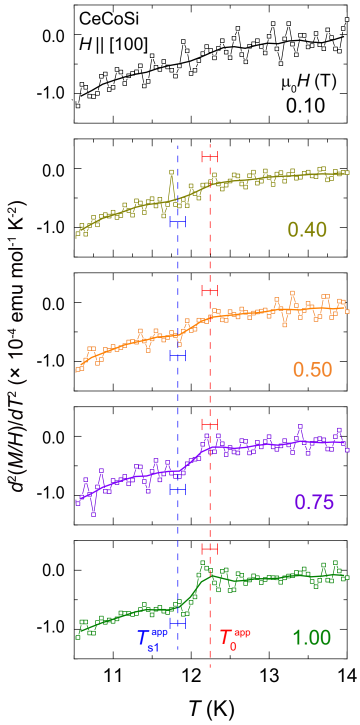


**Fig. 7.** (Color online) Second derivative of $M(T)/H$ in CeCoSi (sample #2) [$= d^2(M(T)/H)/dT^2$] with respect to temperature for $H \parallel [100]$ below 1 T. The solid curves represent the data obtained by the second derivative of the $M(T)/H$ data after interpolation. The dashed lines indicate the apparent transition temperatures $T_0^{app}$ and $T_{s1}^{app}$ (see main text for details).

### *3.1.3 H–T phase diagram*

Figure 5 shows the $H$–$T$ phase diagram of CeCoSi constructed on the basis of the present $\rho$ and $M$ measurements using sample #1 under $H \parallel [110]$. In this phase diagram, $T_0$ and $T_N$ obtained from the previous $C$ measurements at zero magnetic field using sample #1 are also plotted.[15] The $H$–$T$ phase diagram constructed in this study is in good agreement with that reported in previous XRD measurements, although $H_{M1}^{110}$ and $H_{M2}^{110}$ determined in this study are slightly different from those determined in the previous XRD study.[24] It is noteworthy that the $H$–$T$ phase diagram for $H \parallel [110]$ has no $H$-induced phase in the HO state, in contrast to that for $H \parallel [100]$. On the other hand, phases II and III are separated into two and three regions by $H_{M1}^{110}$ and $H_{M2}^{110}$, respectively. The previous XRD measurements revealed that domain alignment occurs at $H_{M1}^{110}$.[24] The domain alignment induced by $H$ in the HO state suggests that the HO of CeCoSi involves the 4$f$ electrons, since a simple structural transition is usually unaffected by $H$. On the other hand, at $H_{M2}^{110}$, it has been suggested that either domain alignment or a change in lattice type occurs.[24]

### *3.2 H || [100] and [110] in the low-H region*

In this section, we focus our attention on how the phase boundary of $T_{s1}$ is drawn on the $H$–$T$ phase diagram, such as, where does $T_{s1}$ meet $T_0$? Therefore, we measured $M$ and $C$ under $H \parallel [100]$ and [110] in CeCoSi (sample #2) to reveal the detailed phase diagrams in the low-$H$ region.

### *3.2.1 Magnetization*

The second derivatives of $M(T)/H$ [$= d^2(M(T)/H)/dT^2$] in CeCoSi (sample #2) with respect to temperature for $H \parallel$ (a)

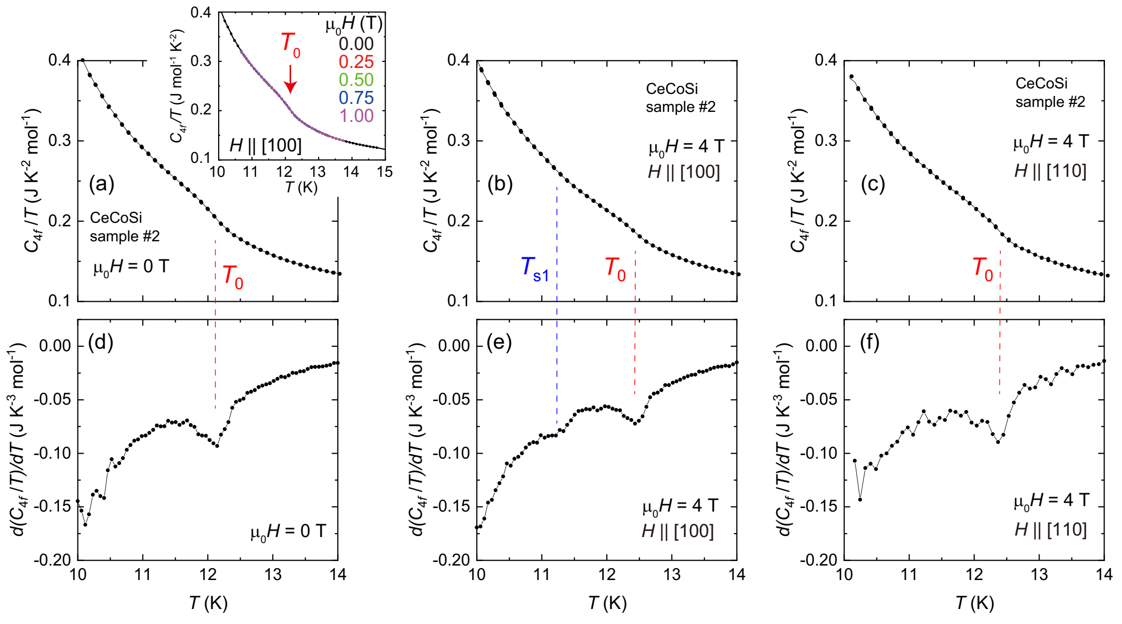


**Fig. 8.** (Color online) Temperature dependence of $C_{4f}/T$ in CeCoSi (sample #2) near $T_0$ at (a) 0 T, (b) 4 T under $H \parallel [100]$, and (c) 4 T under $H \parallel [110]$. $C_{4f}$ is the contribution of $4f$ electrons to specific heat, estimated by subtracting the $C$ of LaCoSi from the $C$ of the present measured sample.[12] The inset of (a) shows $C_{4f}(T)/T$ below 1 T under $H \parallel [100]$. Their first derivatives with respect to temperature are shown in (d)–(f), which were obtained by differentiating the interpolated data of $C_{4f}(T)/T$.

[100] and (b) [110] at 4 T are shown in Figs. 6(a) and 6(b), respectively. For $H \parallel [100]$, the $d^2(M(T)/H)/dT^2$ curve shows a maximum at $T_0$ and a minimum at $T_{s1}$. The $T_0$ determined from the second derivative in sample #2 is in good agreement with that previously reported by Tanida et al.,[12] but slightly lower than that in sample #1 owing to sample dependence. The $T_{s1}$ in sample #2 is also lower than that in sample #1,[15] which would be related to the lower $T_0$ in sample #2. On the other hand, the $d^2(M(T)/H)/dT^2$ curve for $H \parallel [110]$ shows the maximum at $T_0$, but no anomaly corresponding to $T_{s1}$ can be observed. Similar analyses were performed on the measured $M$ data up to 7 T, which are presented in Fig. S1 in SM.[29] $T_0$ increases and $T_{s1}$ decreases with increasing $H$, as summarized in Fig. 9. Note that the $d^2(M(T)/H)/dT^2$ curves for sample #1 for $H \parallel [001]$ show only the maximum at $T_0$, namely, no anomaly corresponding to the $T_{s1}$ transition (see Fig. S2 in SM).[29]

Next, the $d^2(M(T)/H)/dT^2$ curves for $H \parallel [100]$ below 1 T are shown in Fig. 7. The solid curve represents the data obtained by taking the second derivative of the $M(T)/H$ data after interpolation. One can observe the maximum and minimum in the $d^2(M(T)/H)/dT^2$ curves above 0.4 T. The temperatures at which the maximum and minimum are observed are almost independent of $H$, as shown by the dashed lines, although there is an uncertainty of $\pm \sim 0.1$ K. The maximum and minimum become less distinct with decreasing $H$ and cannot be identified below 0.3 T.

At first glance, the observed maximum and minimum seem to correspond to the transitions at $T_0$ and $T_{s1}$, respectively, but cannot simply be interpreted as such. This is because the apparent maximum and minimum appear outside the true maximum and minimum as a result of their superposition (see Fig. S6 in SM).[29] In other words, when $T_0$ and $T_{s1}$ are nearly adjacent, the apparent $T_0$ and $T_{s1}$ ($\equiv T_0^{\mathrm{app}}$ and $T_{s1}^{\mathrm{app}}$) will appear at higher and lower temperatures than the true $T_0$ and $T_{s1}$, respectively. $T_0^{\mathrm{app}}$ and $T_{s1}^{\mathrm{app}}$ are plotted as open circles on the $H$–$T$ phase diagram [Figs. 9(a) and 10] to distinguish them from the true $T_0$ and $T_{s1}$.

### 3.2.2 *Specific heat*

In addition to the $M$ measurements, the $C$ measurements under $H \parallel [100]$ and [110] were also performed to investigate the phase boundaries of $T_0$ and $T_{s1}$. The temperature dependence of $C_{4f}/T$ in CeCoSi (sample #2) near $T_0$ at $\mu_0 H = 0$ T and its first derivative [$= d(C_{4f}/T)/dT$] are shown in Figs. 8(a) and 8(d), respectively. Here, $C_{4f}$ is the contribution of $4f$ electrons to the specific heat, estimated by subtracting the $C$ of LaCoSi from the $C$ of the present measured sample.[12] The $C_{4f}(T)/T$ curve at 0 T shows a broad step-like anomaly at $T_0 \sim 12.1$ K. Here, the value of $T_0$ was determined from the minimum of $d(C_{4f}/T)/dT$. The $C_{4f}(T)/T$ curves for $H \parallel [100]$ below 1 T are hardly affected by the application of $H$, as can be seen in the inset of Fig. 8(a).

Figures 8(b) and 8(c) show the temperature dependence of $C_{4f}/T$ in CeCoSi (sample #2) near $T_0$ at 4 T under $H \parallel [100]$ and [110], respectively. Their first derivatives are also shown in Figs. 8(e) and 8(f), which were obtained by differentiating the interpolated data of $C_{4f}(T)/T$. For [100], the $d(C_{4f}/T)/dT$ curve at 4 T shows the minimum at temperatures corresponding to $T_0$ and $T_{s1}$. This result indicates that the $C_{4f}(T)/T$ curve exhibits a step-like anomaly even at $T_{s1}$, providing thermodynamic evidence that the $T_{s1}$ anomaly represents a phase transition. On the other hand, the first derivative for [110] shows the minimum only at $T_0$; no indication of $T_{s1}$ is observed within the experimental accuracy. Furthermore, similar analyses were performed on the measured $C$ data up to 5 T, which are presented in Sect. 2 in SM.[29] The $T_0$ and $T_{s1}$ determined in the present $C$ measurements are summarized in the $H$–$T$

phase diagrams (Figs. 9 and 10). The error for each transition point was determined by the full width at half maximum of the peak anomaly in $d(C_{4f}/T)/dT$.

### 3.2.3 *H–T phase diagram*

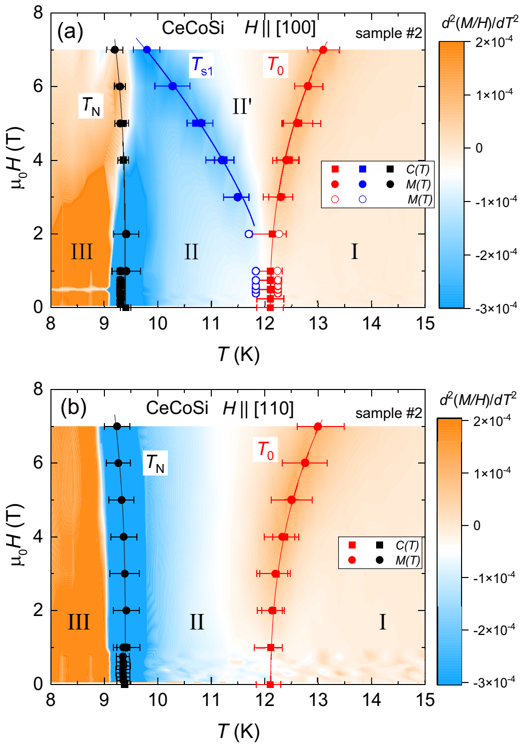


**Fig. 9.** (Color online) *H–T* phase diagrams of CeCoSi between 8 and 18 K below 7 T constructed on the basis of the present *M* and *C* measurements using sample #2 under *H* || (a) [100] and (b) [110]. In these figures, a contour plot of the second derivative of $M(T)/H$ is also presented. Here, the PM, HO, and AFM phases are denoted as I, II, and III, respectively. Open circles represent the apparent transition points of $T_0^{\mathrm{app}}$ and $T_{s1}^{\mathrm{app}}$ (see the main text for details). The solid curves are guides for the eye.

Figures 9(a) and 9(b) respectively show the *H–T* phase diagrams of CeCoSi for *H* || [100] and [110] between 8 and 15 K, which were constructed on the basis of the present *M* and *C* measurements using sample #2. These figures also include a contour plot of the second derivative of $M(T)/H$, where the reddish color indicates larger values, whereas the bluish color indicates smaller ones. The *H* dependence of $T_0$ is equal between *H* || [100] and [110] in the measured *H* region within the experimental accuracy. $T_{s1}$ approaches $T_0$ with decreasing *H* for *H* || [100], whereas the $T_{s1}$ transition is absent in the phase diagram for *H* || [110].

It is clear from the contour plots that $T_N$ corresponds to the minimum of the second derivative of $M(T)/H$ in most of the measured region. For *H* || [100], the color at $T_N$ changes from bluish to reddish at around 4 T, which reflects the result that the kink at $T_N$ is transformed into the dip anomaly by applying a strong *H*, as shown in Fig. 2. In addition, the $T_{s1}$ phase boundary would meet the $T_N$ phase boundary at about 8 T, suggesting the presence of a polycritical point (PCP).

An enlarged view of the *H–T* phase diagram for *H* || [100] near $T_0$ and $T_{s1}$ is shown in Fig. 10. The estimated $T_0$s from the *C* (red square) and *M* (red circle) measurements are in good agreement above 3 T. Below 2 T, however, they appear to be separated, although the difference is within the error bar. This separation of $T_0$ below 2 T can be explained by the appearance of the apparent transition temperature, as mentioned in Sect. 3.2.1. Note that the larger error bar on the low temperature side of $T_0$ at 1 and 2 T, estimated from the *C* measurements, is likely to be due to the influence of the $T_{s1}$ transition.

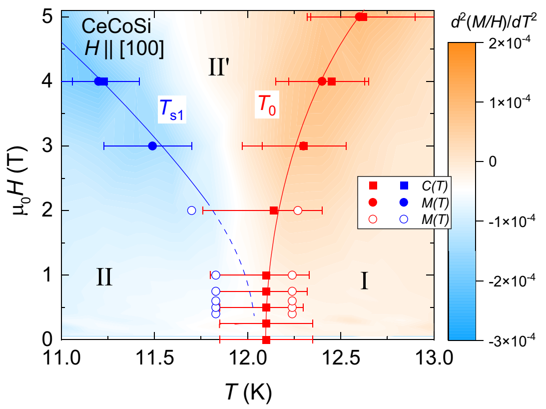


**Fig. 10.** (Color online) An enlarged view of the *H–T* phase diagram for *H* || [100] near $T_0$ and $T_{s1}$ below 5 T. In this figure, a contour plot of the second derivative of $M(T)/H$ is also shown simultaneously. The open circles represent the apparent transition points of $T_0^{\mathrm{app}}$ and $T_{s1}^{\mathrm{app}}$. Their error bars (± ~ 0.1 K) are not shown for clarity. The solid curves are guides for the eye. The blue-dashed curve represents the $T_{s1}$ phase boundary inferred from this study.

The possible appearance of the apparent transition temperatures suggests that the true $T_{s1}$ between 0.4 and 1 T lies between $T_{s1}^{\mathrm{app}}$ and the midpoint between $T_0^{\mathrm{app}}$ and $T_{s1}^{\mathrm{app}}$, that is, approximately between 11.8 and 12.1 K (see Fig. S6 in SM).[29] In addition, the apparent maximum and minimum anomalies in $d^2(M(T)/H)/dT^2$ become weaker with decreasing *H* below 1 T, keeping the distance between $T_0^{\mathrm{app}}$ and $T_{s1}^{\mathrm{app}}$, as shown in Fig. 7. These behaviors suggest that $T_{s1}$ gradually approaches $T_0$ toward zero field,[29] although it is difficult to estimate the intrinsic attenuation of these anomalies near zero field. In Fig. 10, the most likely $T_{s1}$ phase boundary below 2 T is indicated as a dashed curve. The possibility of the $T_{s1}$ phase boundary below 0.4 T will be discussed in Sect. 4.2.

## 4. Discussion

As presented in this paper, we have constructed the *H–T* phase diagrams of CeCoSi for three crystallographic directions using bulk experimental methods and revealed the anisotropic nature of each ordered phase. In this section, we will first give an overview of the *H–T* phase diagram of CeCoSi in Sect. 4.1, and then discuss phases II and II' at low fields in Sect. 4.2. Next, we will present an interpretation of the anisotropic *H–T* phase diagrams based on Landau's theory in Sect. 4.3. Finally, we will briefly discuss some open issues of CeCoSi in Sect. 4.4.

### 4.1 *An overview of the H–T phase diagram*

Several authors have discussed the orderings of CeCoSi at low temperatures, especially for the HO.[12,15,17,21,24,30] Combined with the present experimental findings, we here provide an overview of the characteristics of the $H$–$T$ phase diagram for the following discussions. Figures 11(a)–11(c) show schematics of the possible $H$–$T$ phase diagrams in CeCoSi for $H \parallel [100]$, [110], and [001], respectively.[12,15,24] The dotted curve separating phases II and II' at low fields under $H \parallel [100]$ is the most likely $T_{s1}$ boundary inferred from this study. $T_0$ shifts to the high-temperature side with increasing $H$ for all $H$ directions, with the largest shift for $H \parallel [001]$. The largest shift for $H \parallel [001]$ may be related to the largest magnetic susceptibility for $H \parallel [001]$.[12,15] It is noteworthy that the shift of $T_0$ induced by $H$ is identical between [100] and [110] within the experimental accuracy, although there is a difference in the presence or absence of the $T_{s1}$ transition in the HO state. On the other hand, $T_N$ decreases with increasing $H$, with the effect of $H$ being larger for [001] than for [100] and [110].[15,20] This anisotropy of $T_N(H)$ should reflect the magnetic structure under the triclinic lattice. In addition, several boundaries related to the domain reconstruction are also shown in these figures (dashed line). Note that it has not been concluded whether $H_{M2}^{110}$ for $H \parallel [110]$ is due to domain alignment or a structural change.

The most striking feature is that the HO phase possesses the inner structure called II', which appears only for $H \parallel [100]$. In both the bulk and single-crystal XRD measurements under $H \parallel [100]$, the transitions at $T_0$ and $T_{s1}$ were detected as two successive phase transitions.[15,24] In addition, the XRD measurements under $H \parallel [100]$ indicated that the crystal structure of phase II' is different from that of phase II.[24] On the other hand, for $H \parallel [110]$, $T_{s1}$ appears to be equal to $T_0$ at least up to $\sim 4$ T in the XRD measurements.[24] $T_0$ for $H \parallel [001]$ may also be equal to $T_{s1}$, considering the absence of phase II'.

The $T_{s1}$ phase boundary above 1 T has been determined from various experimental studies,[15,24] where $T_{s1}$ decreases upon the application of $H$ and appears to meet the $T_N$ phase boundary. This result implies the presence of the PCP at ($T$, $\mu_0 H$) $\sim$ (9 K, 8 T). Furthermore, the $H_{M2}^{100}$ anomaly in the AFM phase observed in the previous $M$ measurements under $H \parallel [100]$[15,31] also appears to merge into this PCP. These features suggest that the AFM phase is divided into two regions by $H_{M2}^{100}$: a lower $H$ region called III and a higher $H$ region called III', where the crystal structure of phase III' is considered to be different from the triclinic one of phase III as suggested by the XRD measurements.[24] If all the phase boundaries are of the second order, the PCP is a tetracritical point, but the $B_{M2}^{100}$ anomaly is likely to be a first-order transition because it is accompanied by hysteresis.[15] At present, we cannot exclude the possibility that $T_{s1}$ passes through the $T_N$ line. In this case, the crystal system of III' would be the same as that of III, i.e., triclinic.

### 4.2 Phases II and II' in the low-H region

It is crucial to reveal how the $T_{s1}$ phase boundary behaves near zero field in order to uncover the origin of HO in CeCoSi. This study suggests that $T_{s1}$ approaches $T_0$ with decreasing $H$ at least above 0.4 T. The most likely case is that $T_{s1}$ coincides with $T_0$ at zero field. The validity of this phase boundary is discussed in the next subsection from the view point of Landau's theory. From an ordering model discussed in the next subsection, the $T_0(H)$ and $T_{s1}(H)$ curves are expected to be proportional to the square of the magnetic field at low fields.

Other possibilities for the $T_{s1}$ phase boundary cannot be excluded at this stage. The first is that the $T_{s1}$ phase boundary terminates at a finite field, namely, the presence of a critical point. It indicates the same symmetry between II and II', which is incompatible with the finding that II and II' have different crystal structures.[24] Moreover, the $T_{s1}$ transition would be a second-order phase transition (not a first-order). For this reason, the first case is unlikely.

The second case is that $T_{s1}$ bifurcates from the $T_0$ phase boundary at a finite magnetic field. However, it is unlikely that the $T_{s1}$ phase boundary suddenly bends below 0.4 T and meets the $T_0$ phase boundary.

The third case is that the $T_{s1}$ transition occurs successively at a temperature lower than $T_0$ at zero field. This could be possible when the maximum and minimum anomalies found in the second derivative of $M(T)$ below 2 T are interpreted not as apparent transitions but as true ones. However, this phase diagram requires that the $T_{s1}$ transition exists below $T_0$ even under other $H$ directions. There is no experimental evidence for the existence of the $T_{s1}$ transition below $T_0$ under $H \parallel [110]$ and [001] thus far. For this reason, the third case may also be unlikely.

The reason why the $T_{s1}$ phase boundary cannot be determined in the low-field region from the bulk measurements might be due to domain formation in addition to the very small separation between $T_0$ and $T_{s1}$. Note that there is no experimental indication supporting the presence of the $H$-induced domain selection in the HO phase for $H \parallel [100]$ in the bulk and XRD measurements,[15,24] whereas the magnetic-field-angle-controlled Co-NMR measurements revealed the presence of domain selection above 2 T caused by the $c$-axis components of $H$.[30] Further microscopy measurements at low fields are necessary to confirm the $T_{s1}$ phase boundary we proposed.

### 4.3 Interpretation of the anisotropic phase diagrams based on Landau's theory

It is important to determine whether the HO transition in CeCoSi is a first-order or second-order phase transition, since a primary OP of a second-order phase transition should be described by a single irreducible representation according to Landau's theory. It has been pointed out that the transition at $T_0$ is the second-order phase transition from the continuous splitting of the NMR spectra below $T_0$.[17] In addition, the continuous splitting of the Bragg peaks below $T_0$ and $T_{s1}$ in the XRD measurements suggests that these transitions are of the second order.[24] In the present $C(T)$ measurements, the observed anomalies at $T_0$ and $T_{s1}$ are too indistinct to conclude whether they are of the first or second order. On the other hand, the $H$ variation of $T_0$ and $T_{s1}$ can be explained by the observed behavior in $M(T)$ and $C_{4f}(T)$ at each transition temperature through the Ehrenfest relation for a second-order phase transition [see Sect. 3 in SM for details].[29] Thus, in this subsection, we assume that these transitions are second-order phase transitions in the whole $H$ region.

We assume a single second-order phase transition at $T_0 = T_{s1}$ at zero field. To explain the NM ordered state accompanied by uniform lattice distortion, revealed by the NQR/NMR and XRD measurements,[17,24,30] as well as the in-plane anisotropy of the $H$–$T$ phase diagrams, we focus on the two-dimensional representation $E_g(Q_{yz}, Q_{zx})$ in the $D_{4h}$ point group as the primary OP of HO in CeCoSi. In $D_{4h}$, the

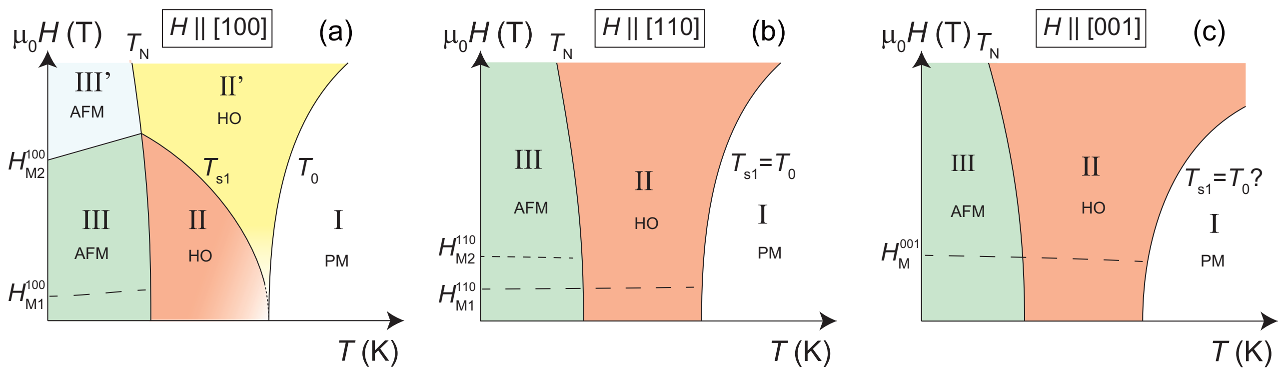


**Fig. 11.** (Color online) Schematics of possible $H$–$T$ phase diagrams of CeCoSi for $H$ || (a) [100], (b) [110], and (c) [001]. These phase diagrams were constructed on the basis of the results of the present and previous studies.[12,15,24] Solid and dashed curves represent the phase transition and domain alignment, respectively. In (a), the dotted curve separating the II and II' phases at low fields is the $T_{s1}$ boundary inferred from this study.

fourth-order coupling of the OPs with the $Q^{\beta1}_{4u}$-type anisotropy can appear in free energy: $b\{(Q^2_{zx} - Q^2_{yz})^2 - (2Q_{zx}Q_{yz})^2\}$. Here, $Q^{\beta1}_{4u}$ is the electric hexadecapole moment [$\propto$ Re$(x + iy)^4$ = $(x^2 - y^2)^2 - (2xy)^2$], $Q_{yz}$ and $Q_{zx}$ are electric quadrupole moments, and $b$ is a constant. The definition and notation of multipolar moments are according to Ref. 32. This anisotropic term is minimized by the $Q_{zx}$ ($Q_{yz}$)-type OP for $b < 0$ or by the $Q_{zx} \pm Q_{yz}$-type OP for $b > 0$. Note that $2Q_{zx}Q_{yz}$ can be rewritten as $\{(Q_{zx} + Q_{yz})/\sqrt{2}\}^2 - \{(Q_{zx} - Q_{yz})/\sqrt{2}\}^2$.

If the OP under $H$ differs from that in the zero field, an $H$-induced phase should appear. The $H$ direction in which the induced phase appears depends on the associated OP via biquadratic couplings of $(Q_{zx}, Q_{yz})$ and $(H_x, H_y)$, represented as $c_\pm\{(H^2_x - H^2_y)(Q^2_{zx} - Q^2_{yz}) \pm 4H_xH_yQ_{zx}Q_{yz}\}$. Here, $H_x$ and $H_y$ are magnetic fields for $x$ and $y$ directions, respectively, and $c_\pm$ is a constant. When $H$ is applied along the [100] direction, the $Q^2_{zx} - Q^2_{yz}$ coupling is finite, and thus, either $Q_{zx}$ or $Q_{yz}$ becomes the OP below $T_0$. Under $H$ || [110], the coupling of $2Q_{zx}Q_{yz}$ is finite, and thus, either $Q_{zx} + Q_{yz}$ or $Q_{zx} - Q_{yz}$ becomes the OP below $T_0$. Experimentally, the $H$-induced phase has been observed under $H$ || [100], but not under $H$ || [110]. Therefore, it can be concluded that the zero-field OP is of the $Q_{zx} \pm Q_{yz}$ type. Details of this model will be reported in the future.

### 4.4 Open issues

Recently, a ferroic $Q_{yz} + Q_{zx}$-type quadrupole ordering model has been proposed as an ordering for the HO of CeCoSi from the results of the $H$-driven domain selection in the HO state found in NMR measurements[30] and the uniform lattice distortion found in the XRD measurements.[24] Its primary OP is consistent with the one proposed in this study based on Landau's theory. It should be commented that, in the previous papers, it has been mentioned that the $Q_{yz} + Q_{zx}$-type ordering gives a triclinic lattice distortion.[24,30] However, we insist that the $Q_{yz} + Q_{zx}$-type ordering gives a monoclinic distortion with mirror symmetry with respect to the (110) plane. Achieving the triclinic structure requires two successive second-order phase transitions or a first-order transition, not a single second-order transition. This discrepancy is an issue to be addressed in the future.

The next is the consistency between the experimentally obtained magnetic phase diagrams and the theoretical ones. Yatsushiro and Hayami presented the $H$–$T$ phase diagrams for $H$ || [100] and [001] by assuming $Q_{zx}(Q_{yz})$-type AFQ and in-plane AFM orderings of the local $4f$ electrons on the basis of the crystal and magnetic structures indicated by the XRD and the neutron diffraction measurements.[16,21,24] The calculated phase diagrams roughly reproduce the increase in $T_0$ and the decrease in $T_N$ with increasing $H$, but they fail to reproduce the presence of the $T_{s1}$ transition under $H$ || [100]. The $Q_{yz} \pm Q_{zx}$-type ordering model discussed in this study could reproduce the experimentally obtained $H$–$T$ phase diagrams.

Finally, the consideration based on Landau's theory can provide the OP in each HO phase, but it cannot provide insights into the microscopic origin. As mentioned in the introduction, it is still controversial whether the atomic quadrupole ordering of local $4f$ electrons at $T_0 \sim 12$ K occurs under the large CEF splitting above 100 K, although Yatsushiro and Hayami have indicated its possibility by tuning the quadrupole interaction.[21]

The essential contribution of $4f$ electrons to HO in CeCoSi is suggested by the experimental results indicating the absence of HO in LaCoSi, the anisotropic $H$–$T$ phase diagrams in CeCoSi, and the effect of pressure on HO.[11–13,24] On the other hand, the presence of lattice distortions on the order of $10^{-4}$ associated with HO suggests that structural instability also plays a role.[24] In addition, recent infrared spectroscopy measurements have suggested that HO is accompanied by a modification in the electronic structure near the Fermi level,[25] which may be the Co-$3d$ conduction band modulation. Very recently, a $f$-electron charge density wave driven by the Ruderman–Kittel–Kasuya–Yosida interaction has also been theoretically proposed as a new ordering model.[22] A comprehensive understanding of the interplay among phonon instability, Co-$3d$ conduction band instability, and the degrees of freedom of local $4f$ electrons will be necessary to solve the mystery of HO in CeCoSi.

## 5. Summary

We have reported the results of $M$, $\rho$, and $C$ measurements of single crystals of CeCoSi under $H$ applied in parallel to the tetragonal [100] and [110] directions, which were performed to construct detailed $H$–$T$ phase diagrams from the viewpoint of bulk properties. The present measurements up to 14 T extended the $H$ region of the phase diagram for $H$ || [110] from that reported in the previous XRD measurements performed up to 6 T.[24] The bulk measurements also confirmed the absence of $T_{s1}$ transitions under $H \parallel [110]$. Considering the superposition of the maximum at $T_0$ and the minimum at $T_{s1}$ in $d^2(M(T)/H)/dT^2$ for $H \parallel [100]$, it is suggested that $T_{s1}$ approaches $T_0$ with decreasing $H$ at least above 0.4 T. In addition, the $H$ variation of $T_{s1}$ and $T_0$ would be related to the observed behavior in $M(T)$ and $C_{4f}(T)$ at each transition temperature through the Ehrenfest relation.

Furthermore, we summarized the experimentally obtained $H$–$T$ phase diagrams of CeCoSi for the $H$ directions of [100], [110] and [001], and discussed the anisotropy of these magnetic phase diagrams on the basis of Landau's theory. Considering the absence of the $H$-induced phase under [110] and [001] and the possible second-order phase transitions, it is likely that $T_{s1}$ coincides with $T_0$ at zero field. From the viewpoint of Landau's theory, these phase diagrams can be explained by the $Q_{zx} \pm Q_{yz}$-type ordering. This ordering has the same OP as the $Q_{yz} + Q_{zx}$-type ferroquadrupole ordering proposed from the previous NMR and XRD measurements.[24,30) However, in the $Q_{zx} \pm Q_{yz}$-type ordering, the crystal structure of the HO state should be monoclinic, not triclinic as previously proposed. It is necessary to further investigate the crystal structure in the HO phase and to determine the magnetic phase diagrams near zero magnetic field by microscopy measurements.

**Acknowledgments** The authors are grateful to T. Matsumura, M. Manago, H. Kotegawa, H. Harima, M. Yatsushiro, S. Hayami, and H. Kusunose for their helpful comments. The present research was supported by JSPS KAKENHI Grant Numbers JP15H05882, JP15H05885(J-Physics), JP18H03683(A), JP20K03825(C), JP23K03294(C), and JP21H01031. This study was also partly supported by Hokkaido University, Global Facility Center (GFC), Advanced Physical Property Open Unit (APPOU), funded by MEXT under the "Support Program for Implementation of New Equipment Sharing System", Grant Numbers JPMXS0420100316, JPMXS0420100317, JPMXS0420100318, and JPMXS0420100319.


1) J. A. Mydosh and P. M. Oppeneer, Rev. Mod. Phys. **83**, 1301 (2011).
2) J. A. Mydosh, P. M. Oppeneer, and P. S. Riseborough, J. Phys.: Condens. Matter **32**, 143002 (2020).
3) R. Shiina, H. Shiba, and P. Thalmeier, J. Phys. Soc. Jpn. **66**, 1741 (1997).
4) T. Onimaru and H. Kusunose, J. Phys. Soc. Jpn. **85**, 082002 (2016).
5) T. Sakakibara, T. Tayama, T. Onimaru, D. Aoki, Y. Ōnuki, H. Sugawara, Y. Aoki, and H. Sato, J. Phys.: Condens. Matter **15**, S2055 (2003).
6) T. Onimaru, T. Sakakibara, A. Harita, T. Tayama, D. Aoki, and Y. Ōnuki, J. Phys. Soc. Jpn. **73**, 2377 (2004).
7) T. Matsumura, S. Nakamura, T. Goto, H. Amitsuka, K. Matsuhira, T. Sakakibara, and T. Suzuki, J. Phys. Soc. Jpn. **67**, 612 (1998).
8) R. Shiina, H. Shiba, and O. Sakai, J. Phys. Soc. Jpn. **68**, 2105 (1999).
9) J. Kitagawa, N. Takeda, M. Ishikawa, T. Yoshida, A. Ishiguro, N. Kimura, and T. Komatsubara, Phys. Rev. B **57**, 7450 (1998).
10) O. I. Bodak, E. I. Gladyshevskii, and P. I. Kripyakevich, J. Struct. Chem. **11**, 283 (1970).
11) H. Tanida, Y. Muro, and T. Matsumura, J. Phys. Soc. Jpn. **87**, 023705 (2018).
12) H. Tanida, K. Mitsumoto, Y. Muro, T. Fukuhara, Y. Kawamura, A. Kondo, K. Kindo, Y. Matsumoto, T. Namiki, T. Kuwai, and T. Matsumura, J. Phys. Soc. Jpn. **88**, 054716 (2019).
13) E. Lengyel, M. Nicklas, N. Caroca-Canales, and C. Geibel, Phys. Rev. B **88**, 155137 (2013).
14) B. Chevalier and S. F. Matar, Phys. Rev. B **70**, 174408 (2004).
15) H. Hidaka, S. Yanagiya, E. Hayasaka, Y. Kaneko, T. Yanagisawa, H. Tanida, and H. Amitsuka, J. Phys. Soc. Jpn. **91**, 094701 (2022).
16) S. E. Nikitin, D. G. Franco, J. Kwon, R. Bewley, A. Podlesnyak, A. Hoser, M. M. Koza, C. Geibel, and O. Stockert, Phys. Rev. B **101**, 214426 (2020).
17) M. Manago, H. Kotegawa, H. Tou, H. Harima, and H. Tanida, J. Phys. Soc. Jpn. **90**, 023702 (2021).
18) J. M. Effantin, J. Rossat-Mignod, P. Burlet, H. Bartholin, S. Kunii, and T. Kasuya, J. Magn. Magn. Mater. **47&48**, 145 (1985).
19) T. Tayama, T. Sakakibara, K. Kitami, M. Yokoyama, K. Tenya, H. Amitsuka, D. Aoki, Y. Ōnuki, and Z. Kletowski, J. Phys. Soc. Jpn. **70**, 248 (2001).
20) T. Kanda, H. Ishikawa, S. Imajo, K. Kindo, H. Tanida, and Y. Kohama, Phys. Rev. B **109**, 174402 (2024).
21) M. Yatsushiro and S. Hayami, J. Phys. Soc. Jpn. **91**, 104701 (2022).
22) T. Yamada, Y. Yanagi, and K. Mitsumoto, J. Phys. Soc. Jpn. **93**, 053703 (2024).
23) H. Tanida, H. Matsuoka, Y. Kawamura, and K. Mitsumoto, J. Phys. Soc. Jpn. **92**, 044703 (2023).
24) T. Matsumura, S. Kishida, M. Tsukagoshi, Y. Kawamura, H. Nakao, and H. Tanida, J. Phys. Soc. Jpn. **91**, 064704 (2022).
25) S.-i. Kimura, H. Watanabe, S. Tatsukawa, and H. Tanida, J. Phys. Soc. Jpn. **92**, 043704 (2023).
26) Y. Kawamura, H. Tanida, R. Ueda, J. Hayashi, K. Takeda, and C. Sekine, J. Phys. Soc. Jpn. **89**, 054702 (2020).
27) Y. Kawamura, K. Ikeda, A. Dalan, J. Hayashi, K. Takeda, C. Sekine, T. Matsumura, J. Gouchi, Y. Uwatoko, T. Tomita, H. Takahashi, and H. Tanida, J. Phys. Soc. Jpn. **91**, 064714 (2022).
28) In the previous paper, the transition point was defined as $B_x$.[15] In this paper, to avoid confusion, we use the notation $T_{s1}$ as defined by Matsumura et al.[24]
29) See Supplemental Materials at [URL will be inserted by publisher]: determination of $T_0$ and $T_{s1}$ from $d^2(M(T)/H)/dT^2$ in Sect. 1, specific heat data under $H \parallel [100]$ and [110] on the sample #2 of CeCoSi in Sect. 2, interpretation of the $T_{s1}$ and $T_0$ phase boundaries based on the Ehrenfest relation in Sect. 3, and simulation of superposition of maximum and minimum in Sect. 4.
30) M. Manago, A. Ishigaki, H. Tou, H. Harima, H. Tanida, and H. Kotegawa, Phys. Rev. B **108**, 085118 (2023).
31) In the previous paper, the anomalies observed in the magnetization processes were defined as $B^a_{M1}$, $B^a_{M2}$, and $B^c_M$.[15] In this paper, we rename them as $H^{100}_{M1}$, $H^{100}_{M2}$, and $H^{001}_M$, respectively.
32) S. Hayami, Y. Yatsushiro, Y. Yanagi, and H. Kusunose, Phys. Rev. B **98**, 165110 (2018).